JOURNAL OF COMPUTATIONAL PHYSICS 60, 41–61 (1985)

A New Approach for Solving the Three-Dimensional Steady Euler Equations. II. Application to Secondary Flows in a Turning Channel*

SIN-CHUNG CHANG AND JOHN J. ADAMCZYK

National Aeronautics and Space Administration, Lewis Research Center, Cleveland, Ohio 44135

Received April 17, 1984; revised September 7, 1984

The solution procedure developed in Part I (S.-C. Chang and J. J. Adamczyk, *J. Comput. Phys.* **59** (1985), 000–000) is discretized and used to obtain inviscid solutions for subsonic flows in a 180° turning channel. It is shown that the current algorithm can accurately predict the behavior of weak secondary flows and is capable of generating solutions for strong secondary flows. Moreover, it is shown that acceptable flow solutions may be obtained after only 10–20 outer loop iterations. © 1985 Academic Press, Inc.

INTRODUCTION

Quite often in fluid flows, one observes a complex cyclic flow pattern on planes normal to the primary flow direction. This flow structure is often referred to as "secondary flow." It is attributed to the streamwise component of vorticity that is generated by the deflection of the primary shear flow due to a boundary surface. The primary driving force behind this phenomenon is the centrifugal pressure gradient in the main flow. The role of viscosity is of secondary importance. Practical examples of hardware in which one finds such flows are turbomachinery blade rows, transition diffuser ducting and fanjet exhaust mixers. It is well known that the prediction and control of secondary flow within these devices can lead to a substantial increase in their aerodynamic performance.

One of the first theoretical efforts at describing the generation of secondary flow was by Squire and Winter [1]. This paper described the generation of secondary flows in a turning channel, with the fluid assumed to be inviscid. Later Hawthorne [2, 3] extended the analysis of Squire and Winter to arbitrary inviscid shear flow. This was then followed by the work of Lakshiminarayana and Horlack [4] in which the effects of viscosity were included. These works provided the theoretical basis of our understanding of secondary flow phenomena. Unfortunately, except for

* Partial results of this paper were presented at AIAA 6th Computational Fluid Dynamics Conference, Danver, Mass., July 13–15, 1983.

0021-9991/85 $3.00

the case of small entry shear or small flow deflection, these analyses do not provide a solution procedure for general secondary flows. To circumvent the difficulty, many researchers have attempted to integrate directly various approximated forms of the Navier–Stokes equations by numerical procedures [5–7]. A notable exception is the work of Abdallah and Hamed [8]. They have analyzed the steady, rotational, inviscid and incompressible flow in a 90° turning channel by solving the continuity equation and two components of the steady Helmholtz equations [9].

In this paper, the solution procedure developed in Part I (the preceding paper) is used to obtain inviscid solutions for subsonic flows and incompressible flows in a 180° turning channel. The problem definition is given in Section I and the Appendix. The finite difference methods are described in Section II. The results of several subsonic flow computations are presented in Section III to illustrate the development of secondary flow in a turning channel. For a weak secondary flow at low Mach numbers, the computed results are shown to be in excellent agreement with the theoretical prediction of Squire and Winter. For large secondary flows two cases were analyzed, the first being the generation of secondary flow due to inlet velocity shear, the second being the generation of secondary flow due to inlet temperature shear. Both cases resulted in the generation of significant nonlinear effects which caused the flow pattern to take on a turbulent-like structure. The results of the incompressible flow computations are not presented since they reveal no new feature. Finally, also in Section III, the efficiency of the current algorithm is assessed using the convergence histories of both the inner and outer iteration loops.

I. Problem Definition

With the aid of Appendix A, we define in this section the channel geometry (Fig. 1a) and the boundary conditions associated with our flow problems. To proceed, a parallelepiped (Fig. 1b) in computational space is defined by

$$a \leqslant x^1 \leqslant b, \qquad c \leqslant x^2 \leqslant d, \qquad \text{and} \qquad 0 \leqslant x^3 \leqslant e \tag{I.1}$$

where the coordinates (x^1, x^2, x^3) refer to computational space and a, b, c, d, and e are geometric parameters to be specified later. The turning channel is generated from the parallelepiped using the transformation $(0 < x^2 < 1)$

$$e^{\pi \bar{x}^1} = \tfrac{1}{2}(\cosh(\pi x^1) - \cos(\pi x^2)) \tag{I.2}$$

$$\cos\left(\frac{\pi \bar{x}^2}{2}\right) = \frac{\sqrt{2}\sinh(\pi x^1/2)\cos(\pi x^2/2)}{\sqrt{\cosh(\pi x^1) - \cos(\pi x^2)}} \tag{I.3}$$

$$\bar{x}^3 = x^3 \tag{I.4}$$

where the coordinates $(\bar{x}^1, \bar{x}^2, \bar{x}^3)$ refer to physical space. It sould be noted that the

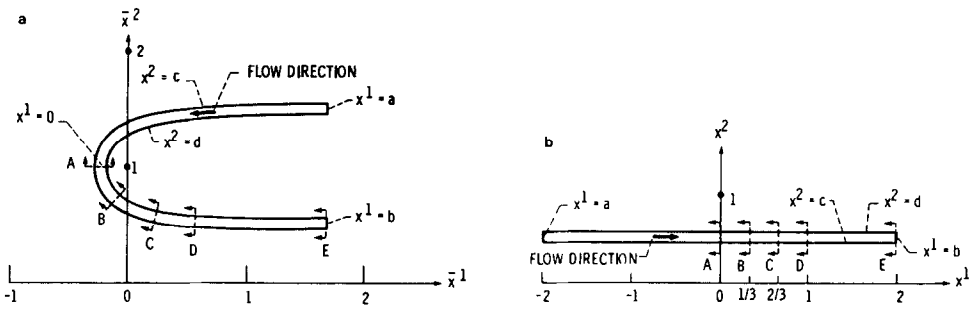

FIG. 1. A turning channel. (a) The physical space ($\bar{x}^3$ is suppressed). (b) The computational space (x^3 is suppressed).

transformation between $Z \equiv (\bar{x}^1, \bar{x}^2)$ and $W \equiv (x^1, x^2)$ is a conformal transformation defined by

$$Z = (2/\pi) \ln(\sinh(\pi W/2)). \tag{I.5}$$

According to Eqs. (I.2) to (I.4), the values of the metric tensor in computational space is given by

$$g_{ij} = \begin{pmatrix} v & 0 & 0 \\ 0 & v & 0 \\ 0 & 0 & 1 \end{pmatrix} \tag{I.6}$$

where

$$v = \frac{\cosh(\pi x^1) + \cos(\pi x^2)}{\cosh(\pi x^1) - \cos(\pi x^2)}. \tag{I.7}$$

As a result, $g_{ij} \to \delta_{ij}$ (Kronecker delta symbol) as $|x^1| \to +\infty$. Therefore, in a region where $|x^1|$ is sufficiently large, the flow equations, the flow description and the channel geometry as viewed from both computational and physical spaces are identical. We shall assume that both the inlet and exit planes lie in such a region.

Assuming a parallel entrance flow, it is shown in the Appendix that the inlet conditions can be specified by an arbitrary axial velocity distribution, an arbitrary temperature distribution and a uniform pressure distribution. For the current investigation, the inlet conditions are explicitly given by (since $v \sim 1$ at the inlet, these conditions can be given directly in computational space)

$$V^1 = V_c \cdot u(x^3, \delta_v), \qquad V^2 = V^3 = 0 \tag{I.8}$$

$$T = T_c \cdot u(x^3, \delta_t) \tag{I.9}$$

$$P = P_c. \tag{I.10}$$

Here V_c, T_c, P_c, δ_v, and δ_t are constants and $u(x^3, \delta)$ is defined by

$$u(x^3, \delta) = 1 + \delta \cdot \left(\frac{x^3}{e} - \frac{1}{2} \right) \tag{I.11}$$

where e is the height of the channel. For a given value of δ, u is a normalized linear function of x^3 with its maximum variation given by δ, i.e.,

$$\frac{1}{e} \int_0^e u(x^3, \delta)\, dx^3 = 1 \tag{I.12}$$

and

$$\delta = u(e, \delta) - u(0, \delta). \tag{I.13}$$

As a result of this normalization, the constants V_c and T_c are the average inlet axial velocity and the average inlet temperature.

To simplify the numerical calculations, Eqs. (I.1) to (I.6) of Part I are nondimensionalized using the procedure described in Part I. By a proper choice of the reference state variables P^* and T^*, the constants P_c and T_c can always be assigned a value of

$$P_c = T_c = 1. \tag{I.14}$$

Thus, the inlet flow conditions can be specified solely in terms of V_c, δ_v, and δ_t. It is shown in the Appendix that these variables, in turn, specify the substitute flow inlet conditions and hence enable us to integrate all the hyperbolic equations to be solved in the outer loop.

TABLE I

The Boundary Conditions for $\varphi^{(n)}$, $\sigma^{(n)}$, and ψ_i

	$x^1 = a$	$x^2 = c$ $x^2 = d$	$x^3 = 0$ $x^3 = e$	$x^1 = b$
$\varphi^{(n)}$	$\dfrac{\partial \varphi^{(n)}}{\partial x^1} = 0$	$\dfrac{\partial \varphi^{(n)}}{\partial x^2} = 0$	$\dfrac{\partial \varphi^{(n)}}{\partial x^3} = 0$	$\varphi^{(n)} = 0$
$\sigma^{(n)}$	$\dfrac{\partial \sigma^{(n)}}{\partial x^1} = 0$	$\dfrac{\partial \sigma^{(n)}}{\partial x^2} = 0$	$\dfrac{\partial \sigma^{(n)}}{\partial x^3} = 0$	$\sigma^{(n)} = 0$
ψ_1	$\dfrac{\partial \psi_1}{\partial x^1} = 0$	$\psi_1 = 0$	$\psi_1 = 0$	$\dfrac{\partial \psi_1}{\partial x^1} = -\left(\dfrac{\partial \psi_2}{\partial x^2} + \dfrac{\partial \psi_3}{\partial x^3} \right)$
ψ_2	$\psi_2 = 0$	$\dfrac{\partial \psi_2}{\partial x^2} = 0$	$\psi_2 = 0$	$\dfrac{\partial \psi_2}{\partial x^1} = 0$
ψ_3	$\psi_3 = 0$	$\psi_3 = 0$	$\dfrac{\partial \psi_3}{\partial x^3} = 0$	$\dfrac{\partial \psi_3}{\partial x^1} = 0$

The boundary conditions required for the solution of the Poisson's equations (II.18), (II.23), and (II.25) of Part I are given in Table I. These conditions are consistent with Eq. (II.19) of Part I. As shown in the Appendix, they also are consistent with the inlet conditions, the solid wall boundary condition (Eq. (A.8)), and an exit flow condition which allows the continuous development of secondary flow far downstream of the channel bend.

Finally, it should be noted that the substitute flow is initialized so that the density ρ and the contravariant mass flux vector F^i satisfy the following conditions:

$$\frac{\partial \rho}{\partial x^1} = 0, \qquad \frac{\partial F^1}{\partial x^1} = 0, \qquad F^2 = F^3 = 0. \tag{I.15}$$

These equations coupled with the given inlet distributions for ρ and F^1 uniquely determine the initial values of ρ and F^i within the computational domain. Subsequently, the contravariant velocity field V^i can be evaluated through the relation: $V^i = F^i/(\rho \sqrt{g})$. The flow field so initialized is consistent with the inlet flow conditions, the solid wall boundary condition, and the continuity equation.

II. Finite Difference Methods

The finite difference solutions to the various equations which form the inner and outer loops are constructed using the grid shown in Fig. 2. This grid is channel conforming with uniform spacing in each direction in computational space.

In the inner loop the divergence, grad, and curl are approximated by second order central difference operators in the interior of the computational domain. At the boundaries the normal derivative operator which appears in these expressions is approximated by either a second order forward or backward finite difference operator. The finite difference form of the Laplacian is fixed by the Fast Solver [10] which is used to solve the Poisson equations.

In the outer loop, the hyperbolic equations are numerically integrated using a characteristic marching procedure. This integration procedure will be explained using Eq. (I.20) of Part I as an example. We assume that the computational domain is bounded by four solid walls in x^2 and x^3 directions (see Fig. 3a). We further assume that V^1 is positive everywhere and that all the values of τ are known on the grid plane GP1.

For an interior grid point A on GP2 at which τ is to be evaluated, a point Q' on GP1 is found (see Fig. 3b) such that the vector $\mathbf{Q'A}$ is in the direction of the known velocity vector at A (denoted by $V^i(A)$). The velocity vector at Q' (denoted by $V^i(Q')$) is computed by linearly interpolating (four point bivariate interpolation [11]) the velocity vectors at the four surrounding grid points A', B', C', and D'. The average of $V^i(Q')$ and $V^i(A)$ is then evaluated and set equal to $\tilde{V}^i(A)$. Next a point Q is located on GP1 such that the vector $\mathbf{QA}$ points in the direction of $\tilde{V}^i(A)$. The value of τ at point Q (denoted by $\tau(Q)$) is then found by linear interpolation

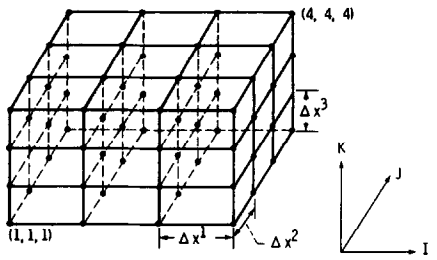

FIG. 2. A uniform grid in computational space (I, J, and K, respectively, are grid indices in x^1, x^2, and x^3 directions).

using the known value of τ at A', B', C', and D'. In the final step, τ is evaluated at point A (denoted by $\tau(A)$) from the equation [12]

$$\tau(A) = \tau(Q) + \frac{\delta x^1}{\tilde{V}^1(A)} \tag{II.1}$$

where δx^1 is the distance between GP1 and GP2. If point A is a boundary grid point, the above procedure becomes two-dimensional (the normal velocity component vanishes at the channel walls).

The stability of the above algorithm is insured by subdividing each grid interval Δx^1 into M equally spaced subintervals. The length of these subintervals, δx^1, is chosen such that the Courant–Friedrich–Lewy stability criteria

$$\frac{|V^2|}{V^1}\frac{\delta x^1}{\Delta x^2} < 1 \qquad \text{and} \qquad \frac{|V^3|}{V^1}\frac{\delta x^1}{\Delta x^3} < 1 \tag{II.2}$$

are satisfied everywhere on the refined grid. The refined grid velocity field is obtained by linearly interpolating the coarse grid velocity field provided by the inner loop.

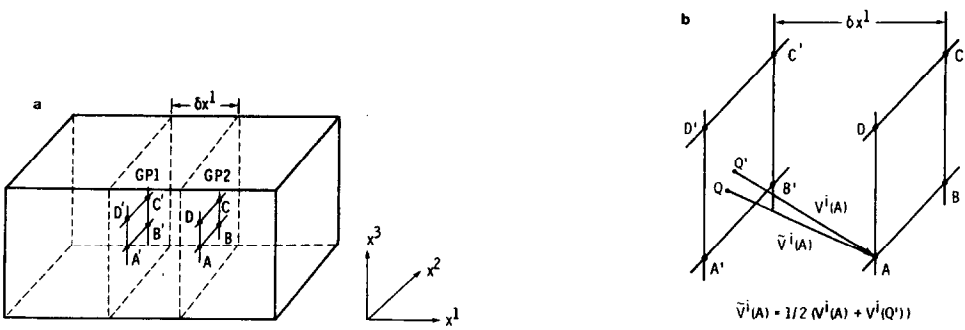

FIG. 3. Marching method for hyperbolic equations. (a) Two adjacent grid planes GP1 and GP2. (b) Construction of a characteristic line.

Once the hyperbolic equations have been solved, the vorticity field is updated using a finite difference representation of the equation

$$\sqrt{g}\,\Omega^i = \varepsilon^{ijk}\frac{\partial}{\partial x^j}\left[\beta\left(h_0\frac{\partial\tau}{\partial x^k}+S\frac{\partial\mu}{\partial x^k}\right)+(\beta-1)\left(\tau\frac{\partial h_0}{\partial x^k}+\mu\frac{\partial S}{\partial x^k}\right)\right] \qquad \text{(II.3)}$$

where β is an arbitrary constant. This equation is equivalent to Eq. (I.19) of Part I. In this study, the finite difference form of the expression on the right side of Eq. (II.3) was obtained in the following way: First, the grad operators inside the bracket are approximated using the corresponding central difference operators. After the quantities inside the bracket have been evaluated at all grid points, the right side of Eq. (II.3) is then evaluated by approximating the curl operator with the corresponding central difference operator. The only exception occurs at the boundaries where the normal derivative is approximated by either a forward or backward second order difference operator. This finite difference form of Eq. (II.3) was chosen such that the central difference form of $\partial(\sqrt{g}\,\Omega^j)/\partial x^j = 0$ (see Eq. (II.21) of Part I) is identically satisfied at all interior grid points.

For a homentropic flow, Eq. (II.3) may be simplified by dropping the terms $S(\partial\mu/\partial x^k)$ and $\mu(\partial S/\partial x^k)$. Similarly, for a homenergetic flow, the terms $h_0(\partial\tau/\partial x^k)$ and $\tau(\partial h_0/\partial x^k)$ may be dropped. Finally, it is noted that the numerical results to be presented in Section III are obtained by assuming $\beta = 0.5$. It has been our experience that the stability of the outer loop iterations is best maintained using this value of β.

III. Numerical Results

This section will be devoted to assessing the ability of the solver to capture the physics of the development of inviscid secondary flows in a turning channel. In order to perform this assessment, three problems were analyzed. For each problem, the values of the parameters previously defined are tabulated in Table II. In addition, the values of the grid parameters NX1, NX2, and NX3 which define the number of grid intervals in the x^1, x^2, and x^3 directions are also tabulated along with the value of NX1S which equals the number of subintervals in a grid interval Δx^1. The values of the parameters c and d were chosen to yield a channel of nearly constant width (approximately equal to $(d-c)$) in physical space. For all three problems the specified inlet flow conditions and channel geometry ensure subsonic flow conditions. The average inlet Mach number (computed using V_c and $T_c = 1$) for the first problem is 0.0845 and therefore the flow is nearly incompressible. For the remaining two problems, its value is 0.4 and the flow is modestly compressible.

To present our numerical results, five stations A, B, C, D, and E (Fig. 1) are chosen along the flow channel. They are channel cross sections defined by $x^1 = 0$, $x^1 = \frac{1}{3}$, $x^1 = \frac{2}{3}$, $x^1 = 1$, and $x^1 = 2$, respectively. These stations are slightly curved in

TABLE II

Flow Problems and Their Defining Parameters

Problem	Geometric parameters					Flow parameters				Grid parameters			
	a	b	c	d	e	γ	V_c	δ_v	δ_t	NX1	NX2	NX3	NX1S
No. 1[a]	−2.0	2.0	0.45	0.55	0.1	1.4	0.1	0.01	0.0	72	6	6	12
No. 2[b]	↓	↓	↓	↓	↓	↓	0.4733	0.2	0.0	144	12	12	12
No. 3[c]	↓	↓	↓	↓	↓	↓	0.4733	0.0	0.3	144	12	12	12

[a] Homentropic and linear.
[b] Homentropic and nonlinear.
[c] Inhomentropic, inhomenergetic, and nonlinear.

physical space. In presenting our results in physical space, we shall neglect the effect of surface curvature and consider these stations to be flat.

The first problem was constructed to examine the ability of the solver to reproduce the theoretical results of incompressible weak secondary flow theory. For this problem the specified inlet flow conditions lead to the establishment of a homentropic flow. Thus this flow was calculated without the aid of the Munk–Prim substitution principle. For the limiting case of incompressible weak secondary flow. Squire and Winter [1] derived the expression

$$\xi = 2\Omega_0 \theta \tag{III.1}$$

for the growth of secondary vorticity along a streamline. In this equation, Ω_0 is the inlet vorticity of the streamline, ξ is the secondary vorticity at any point on the streamline where the local angle of deflection (i.e., the angle between the streamline direction at the inlet and its direction at a point in the channel) is θ. For the chosen

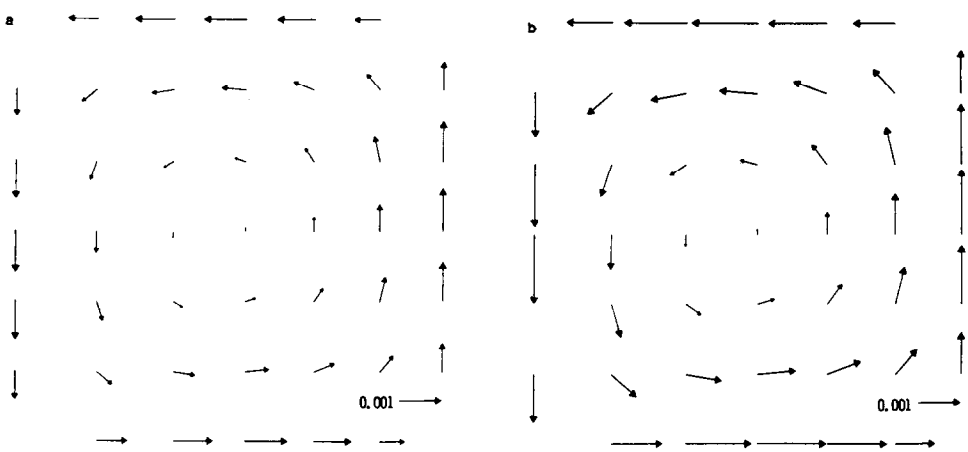

FIG. 4. Secondary velocity field for Problem 1. (a) Station A. (b) Station B.

TABLE III

Numerical Values of $\xi/(2\Omega_0\theta)$ at Various Stations after 40 Outer Loops Iterations (Problem No. 1, $\Omega_0 = 0.1$)

	Station				
	A	*B*	*C*	*D*	*E*
θ (radian)	1.5708	2.4666	2.8965	3.0552	3.1379
$\xi/(2\Omega_0\theta)$	0.9978	0.9967	0.9933	0.9879	0.9682

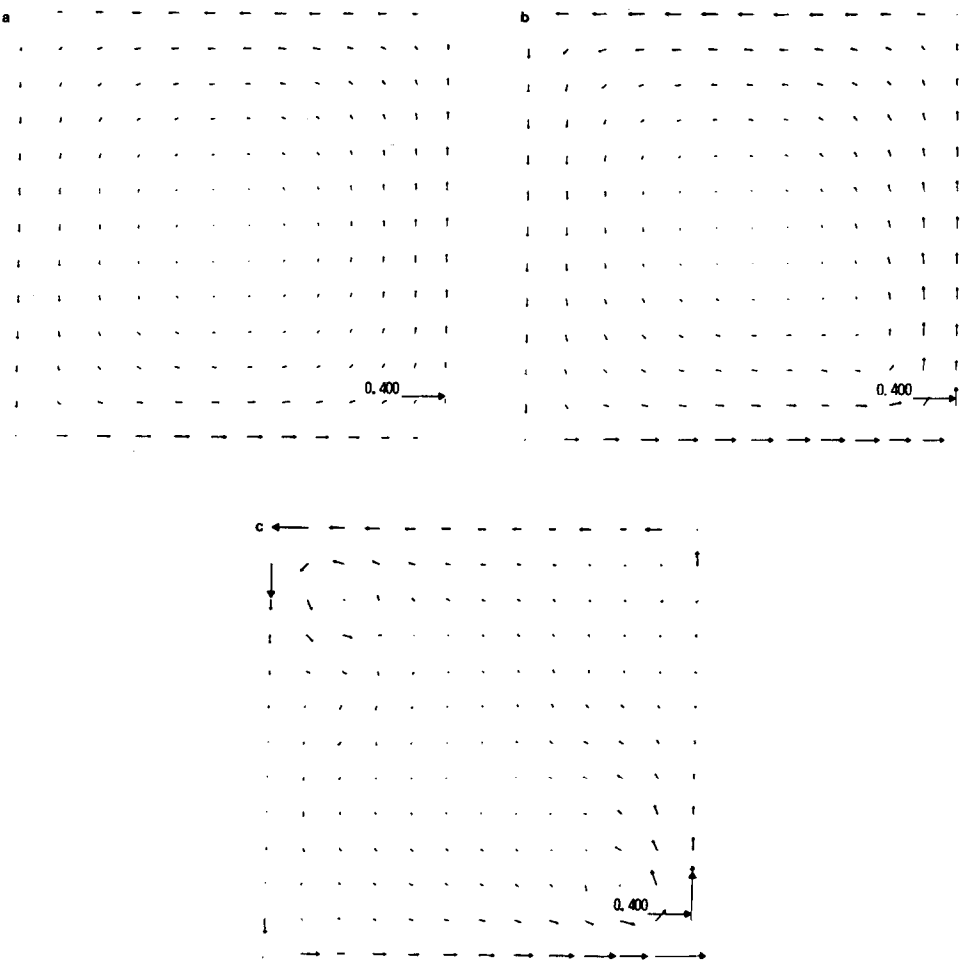

FIG. 5. Secondary velocity field for Problem 2. (a) Station A. (b) Station B. (c) Station D.

channel the values of θ are more or less constant across any cross section. Since the imposed inlet flow field is such that all streamlines share a common value of Ω_0 ($\Omega_0 = \delta_v/e$ for the current problems) it is seen that ξ should be nearly uniform across any cross section of the channel.

The secondary velocity fields at Stations A and B for the first problem are shown in Fig. 4. Comparing the magnitude of the displayed velocity vectors to the inlet area averaged velocity of $V_c = 0.1$ (the length scale of the vectors is indicated by a standard vector at the bottom-right corner of each plot), they are seen to be very small. Thus the theory of Squire and Winter should be applicable to this problem. Both figures show the generated secondary velocity field exhibits a solid body rotational pattern over most of the cross section, which indicates the secondary vorticity is indeed nearly uniform over each cross section. The only exception occurs in the corner regions where a solid body rotation of fluid is impossible.

Furthermore, Fig. 4 indicates that one may view the line defined by $x^2 = 0.5$ and $x^3 = 0.05$ (according to Eq. (I.1) and Table II, this line passes through the central grid point at all cross sections) as a streamline since the secondary velocity is nearly zero along this line. At the five points where this approximate streamline intersects Stations A, B, C, D, and E, the values of θ and $\xi/(2\Omega_0\theta)$ for the first problem are tabulated in Table III. The numerical results are seen to be in excellent agreement with Eq. (III.1). These results also indicate that, as the flow proceeds further down the channel and the secondary velocity grows larger, nonlinear effects begin to come into play and the agreement between linear theory and numerical results deteriorates.

For the second problem, a significantly larger value of inlet velocity shear was chosen to assess the ability of the solver to capture the physics associated with large secondary flows. Figure 5 shows the secondary velocities that developed at Stations A, B, and D. At Station A, the secondary velocity field is well established, exhibiting the solid body rotation pattern predicted by the linear analysis of Squire and Winter. As the flow proceeds further around the bend, the local secondary velocity field near the four corners grows in magnitude, with a maximum approaching the average inlet velocity $V_c = 0.4733$. This flow structure can no longer be predicted by the linear theory of Squire and Winter. At Station D which lies well downstream of the channel bend, the nonlinear behavior grows more evident as two additional vortices appear in the upper-left and lower-right corners. Further downstream from Station D, the secondary flow field becomes ill-defined and begins to take on the appearance of turbulence (not shown).

To study other aspects of this homentropic flow, the contours of constant total pressure P_0 at Stations A, B, and D were computed and are shown in Fig. 6. Since a surface of constant P_0 is a stream surface (see Eq. (I.12) of Part I), these illustrations also represent the cross-sectional views of several stream surfaces. For the current problem, the inlet flow conditions vary only in the x^3 direction. Therefore, the stream surfaces are horizontal at the channel entrance. The contour values of P_0 were chosen to yield contours which coincide with the horizontal grid lines at the entrance to the channel.

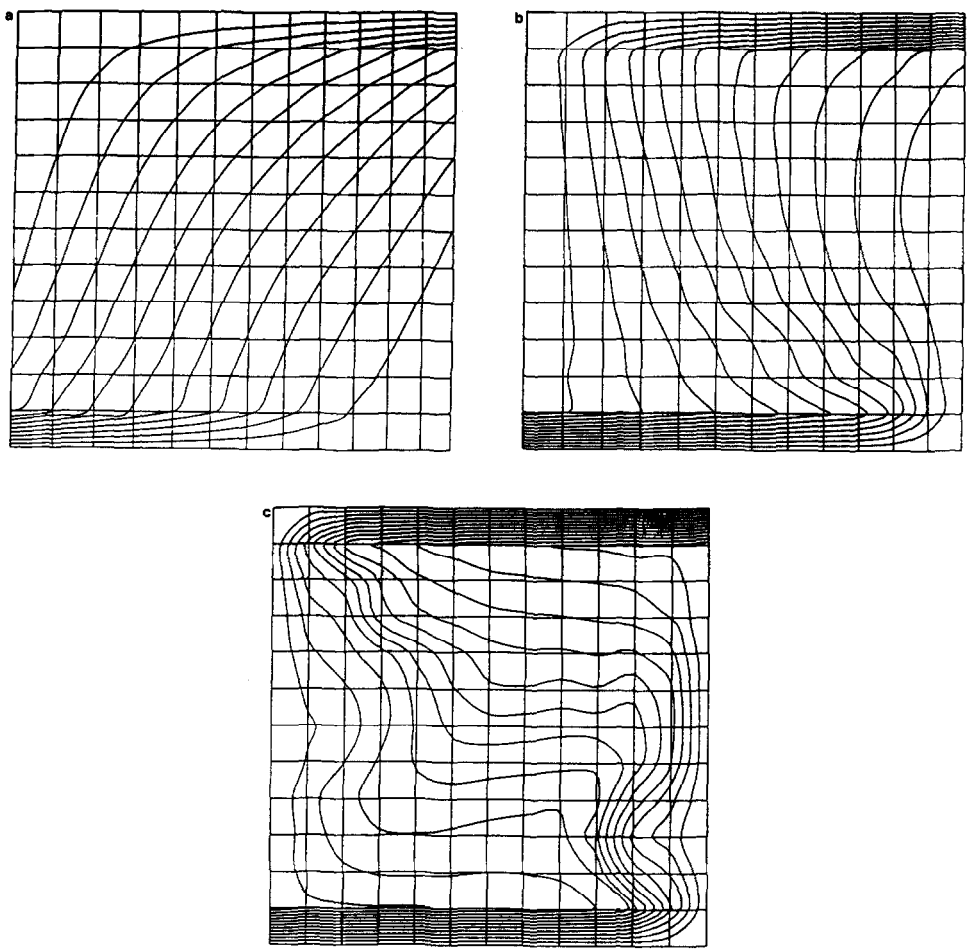

FIG. 6. Total pressure contours for Problem 2. (a) Station A. (b) Station B. (c) Station D.

As the flow proceeds down the channel, the stream surfaces are rotated by the secondary velocity field to near vertical slighty downstream of Station A. The only exception occurs at the upper-right and lower-left corner regions where they tend to become clustered. This phenomenon can be explained by recalling that every stream

down the channel, the fluid particles initially attached to the right (left) side wall will remain attached as long as streamline bifurcation does not take place. In addition these particles are transported toward the top or bottom walls by the secondary velocity field. Since the top and bottom walls are stream surfaces on which P_0 is either a maximum or a minimum (i.e., maximum on the top wall, minimum on the bottom wall), the fluid particles on the side walls can never reach

the top or bottom unless equation (I.12) of Part I is violated. They become stagnated when viewed in the cross-sectional plane. This leads to the clustering phenomena depicted in the figure. At Station D, the total pressure contour becomes highly contorted and also shows additional clustering in the upper-left and lower-right corner regions.

The secondary flows which we have discussed so far have all been generated as a result of an inlet velocity shear. In Problem 3, we examine the secondary flow as generated by a temperature shear. The entering velocity field is uniform, while the inlet temperature and entropy vary in only the x^3 direction. The solution to this general Munk–Prim problem was obtained assuming the substitute flow to be homentropic.

The resulting secondary velocity fields developed at Stations A, B, and D are shown in Fig. 7. Comparing these results with those on Fig. 5, it is seen that the secondary velocity fields are very similar except for their sense of rotation. This result can be explained by recalling that the streamline pattern for Problem 3 is identical to that of the homentropic substitute flow from which it was constructed. This substitute flow has a negative velocity shear (i.e., axial velocity decreases in the x^3 direction) and uniform temperature and entropy distributions at the channel inlet. These inlet flow conditions with the exception of the sign of the inlet velocity shear are very similar to those for Problem 2. This accounts for their close resemblance. Furthermore, examination of the contours of constant total pressure (not shown) further corroborated the close resemblance of these two problems.

This section is concluded with a discussion on the convergence histories of the inner and outer loops. To proceed, let

$$R^{(l)}(I) \overset{\text{def}}{=} \left[\sum_{J,k=1} |\mathbf{V}^{(l+1)}(I, J, K) - \mathbf{V}^{(l)}(I, J, K)|^2 \right]^{1/2} \quad \begin{pmatrix} l = 0, 1, 2, \ldots \\ I = 1, 2, 3, \ldots \end{pmatrix}. \tag{III.2}$$

Here $\mathbf{V}^{(l)}(I, J, K)$ may denote the velocity vector at the grid point (I, J, K) (see Fig. 2) after l iterations during a pass through the inner loop. It may also denote a similar vector after l outer loop iterations (i.e., l passes through the inner loop). Furthermore, it should be noted that the summation inside the bracket runs through the grid points with a common value of I. The parameter $R^{(l)}(I)$ is an overall measure of the change of the velocity field at a grid plane of index I during the $(l+1)$th iteration. A similar parameter which measures the change of the entire velocity field is

$$R^{(l)} \overset{\text{def}}{=} \left[\sum_{I,J,k=1} |\mathbf{V}^{(l+1)}(I, J, K) - \mathbf{V}^{(l)}(I, J, K)|^2 \right]^{1/2} \quad (l = 0, 1, 2, \ldots). \tag{III.3}$$

Here the summation runs through all the grid points. Moreover, to measure the convergence after l iterations, one introduces

$$O^{(l)}(I) \overset{\text{def}}{=} -\log(R^{(l)}(I)/R^{(0)}(I)) \qquad (l = 0, 1, 2, \ldots) \tag{III.4}$$

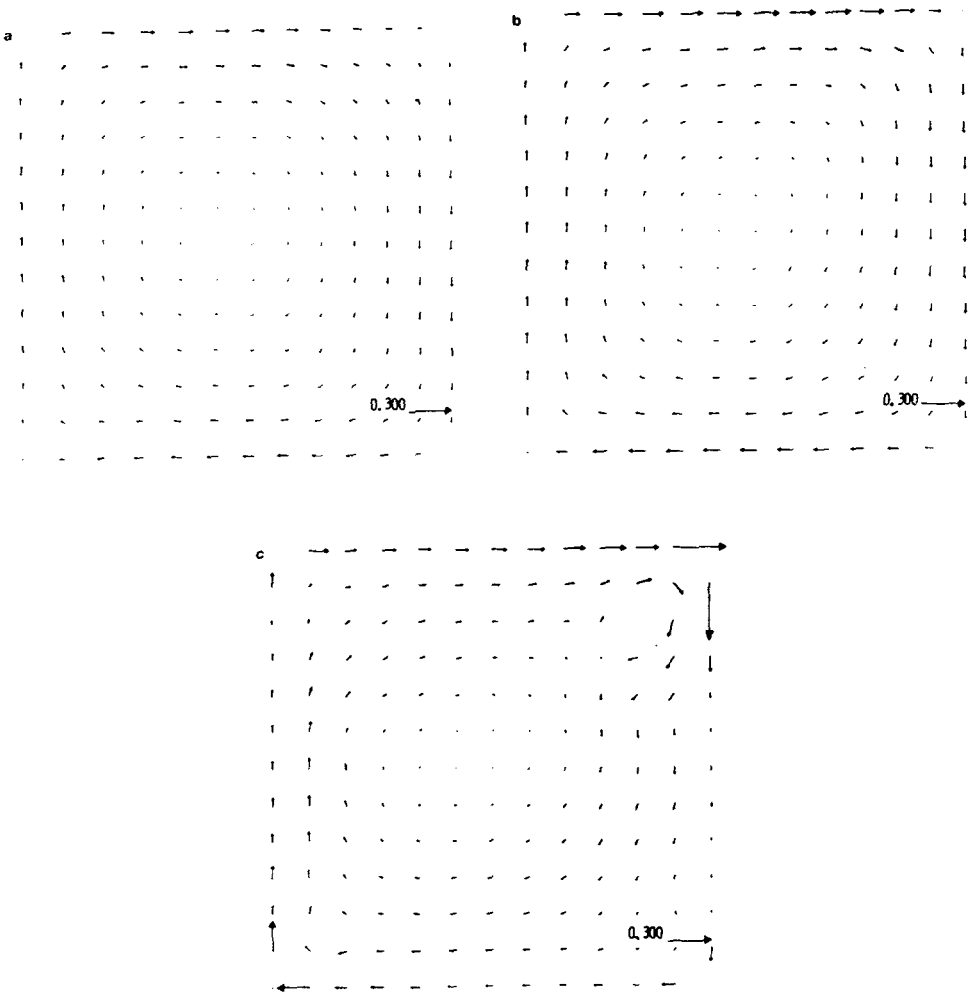

FIG. 7. Secondary velocity field for Problem 3. (a) Station A. (b) Station B. (c) Station D.

and

$$O^{(l)} \stackrel{\text{def}}{=} -\log(R^{(l)}/R^{(0)}) \qquad (l=0, 1, 2,...). \tag{III.5}$$

It is clear that $O^{(l)}(I)$ and $O^{(l)}$, respectively, are the orders of magnitude in the reduction of the values of $R^{(l)}(I)$ and $R^{(l)}$ versus their values at $l=0$.

For the inner loop iterations, we shall assume that $l=n/2$ where n is the inner loop iteration number referred to in Part I. In other words, a combined application of Scheme A and Scheme B (see Section II.3 of Part I) is counted as one iteration whenever the iteration number l is referred to. This new way of counting l is consistent with the fact that the function G defined in Eqs. (B.10) and (B.11) of Part I

is an amplification factor per combined application of Scheme A and Scheme B. With this understanding, the histories of $O^{(l)}$, $O^{(l)}(37)$, $O^{(l)}(55)$, and $O^{(l)}(73)$ for Problem 1 during the first pass through the inner loop are shown in Fig. 8a. It is seen immediately that the inner loop iterations converge rapidly and the convergence histories at Stations A, D, and E (for Problem 1, these stations correspond to the grid planes with $I=37$, 55, and 73, respectively) are distinctly different. These features, as we shall see, may be qualitatively explained by using the results of a stability analysis presented in Appendix B of Part I.

To proceed, it is noted that the function G_0 defined in Eq. (B.14) of Part I is a theoretical parameter measuring the local amplification rate (per iteration) of a high wave number disturbance. With the aid of Eqs. (I.6) and (I.7), this parameter can be expressed as

$$G_0 = \Gamma(x^1, x^2) \stackrel{\text{def}}{=} \frac{\cos^2(\pi x^2)}{\cosh^2(\pi x^1) - \cos^2(\pi x^2)}. \tag{III.6}$$

Noting that $\Gamma_m(c, d) \stackrel{\text{def}}{=}$ the maximum value of $\Gamma(x^1, x^2)$ in the domain defined by

$$2 \geqslant x^1 \geqslant -2 \qquad \text{and} \qquad d \geqslant x^2 \geqslant c \tag{III.7}$$

it is seen from Table IV that $\Gamma(x^1, x^2) \leqslant 2.51 \times 10^{-2}$ within the computational domain for Problem 1. With the interpretation given to $\Gamma(x^1, x^2)$, one would expect the inner loop iterations to converge raidly. This expectation is confirmed by the fact that $O^{(4)} = 5.10$, i.e., the value of $R^{(l)}$, on the average, is reduced by more than one order of magnitude per iteration. Moreover, it is interesting to note that the average increment of $O^{(l)}$ per iteration ($=1.275$) may be qualitatively predicted using the value of $-\log[\Gamma_m(c, d)]$ ($=1.60$).

To study the convergence histories at individual stations, one notes that $\Gamma_m(\xi; c, d) \stackrel{\text{def}}{=}$ the maximum value of $\Gamma(x^1, x^2)$ in the subdomain defined by

$$x^1 = \xi \qquad \text{and} \qquad d \geqslant x^2 \geqslant c. \tag{III.8}$$

As a result, it is seen from Table IV that, for Problem 1, the maximum values of

TABLE IV

Numerical Values of $\Gamma_m(c, d)$ and $\Gamma_m(\xi; c, d)$

	$c=0.45$ $d=0.55$	$c=0.65$ $d=0.75$
$\Gamma_m(c, d)$	2.51×10^{-2} (1.60)	1.0 (0.)
$\Gamma_m(0; c, d)$	2.51×10^{-2} (1.60)	1.0 (0.)
$\Gamma_m(1; c, d)$	1.82×10^{-4} (3.74)	3.73×10^{-3} (2.43)
$\Gamma_m(2; c, d)$	3.41×10^{-7} (6.47)	2.79×10^{-5} (4.55)

Note. The values of $-\log[\Gamma_m(c, d)]$ and $-\log[\Gamma_m(\xi; c, d)]$ are given in parentheses.

$\Gamma(x^1, x^2)$ at Stations A ($x^1 = 0$), D ($x^1 = 1.0$), and E ($x^1 = 2.0$) are 2.51×10^{-2}, 1.82×10^{-4}, and 3.41×10^{-7}, respectively. Based on the interpretation given to $\Gamma(x^1, x^2)$, it is predicted that $O^{(l)}(73) > O^{(l)}(55) > O^{(l)}(37)$. Again, this prediction is confirmed by Fig. 8a. However, the results shown in Fig. 8a also indicate that the initial rapid convergence at Station E eventually is slowed down by slower convergence at other stations. This interdependence between convergence at separate stations obviously cannot be accounted for by a local stability analysis like ours.

To further evaluate the current inner loop stability analysis, a new set of convergence histories is shown in Fig. 8b. These new histories are generated using the same defining parameters as in Problem 1 except that the values of the geometric parameters c and d are changed to $c = 0.65$ and $d = 0.75$. With these changes, the flow channel generated using Eq. (I.5) becomes a converging–diverging turning channel which is shown in Fig. 9. Furthermore, the maximum value of $\Gamma(x^1, x^2)$

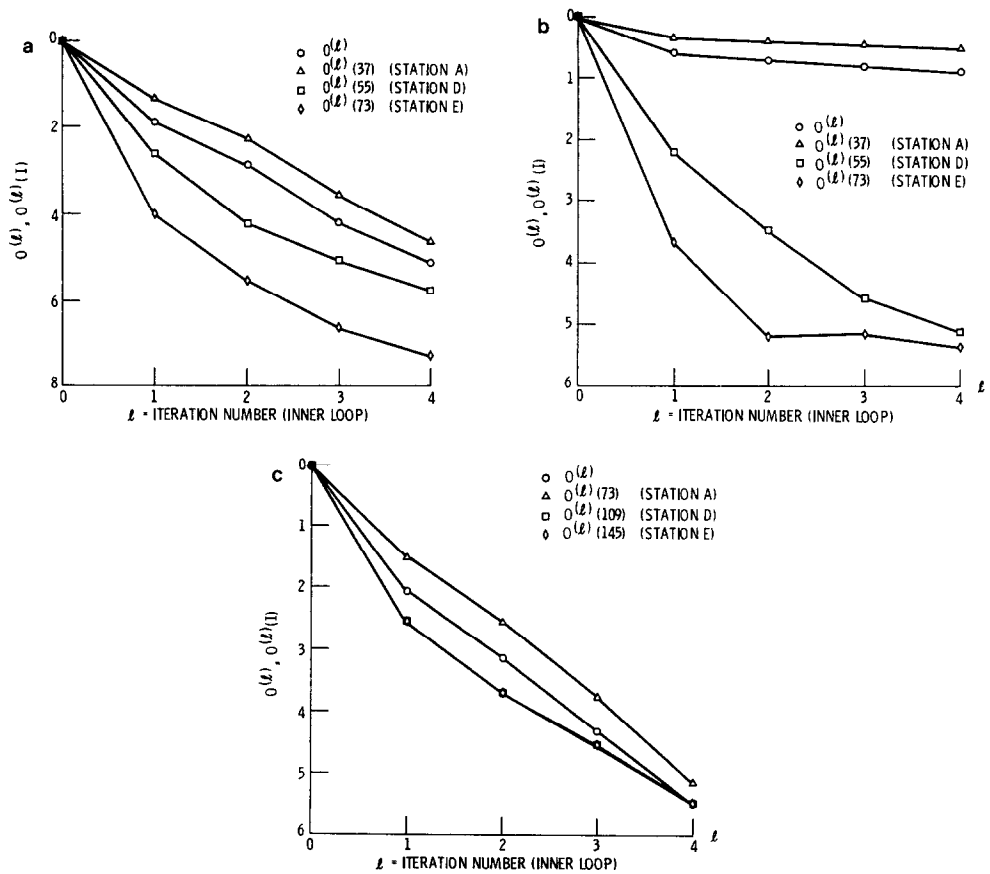

FIG. 8. Convergence histories during the first pass through the inner loop. (a) Problem 1 ($c = 0.45$, $d = 0.55$). (b) Problem 1 with modified computational domain ($c = 0.65$, $d = 0.75$). (c) Problem 2 ($c = 0.45$, $d = 0.55$).

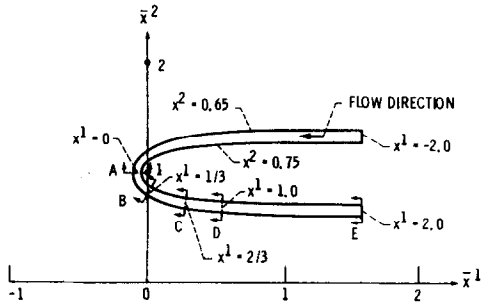

FIG. 9. A converging–diverging turning channel ($\bar{x}^3$ is suppressed).

within the domain of the new channel is elevated to 1 (see Table IV). According to stability condition Eq. (B.15) of Part I, the continuous version of the inner loop iterations is on the verge of instability. This observation correlates very well with the fact that the relation between the parameter $O^{(l)}$ and the iteration number l is represented by a nearly horizontal line. Similarly, the drastically different histories of $O^{(l)}(37)$, $O^{(l)}(55)$, $O^{(l)}(73)$, can also be explained by using the fact that the maximum values of $\Gamma(x^1, x^2)$ at Stations A, D, and E are 1.0, 3.73×10^{-3}, and 2.79×10^{-5}, respectively.

In spite of the fact that the current inner loop stability analysis is based upon several limiting assumptions and intended only for the continuous version of the inner loop iterations, it has been shown that, for a nearly incompressible flow, this analysis is a useful tool for predicting the stability and the convergence rate of a discretized version of the inner loop iterations. Since the current stability analysis assumes that the iterative increments of the mass density are negligible, in principle, this analysis should be of little use in explaining the convergence behavior of the inner loop iterations whenever a compressible flow is involved. However, in reality, the above assessment turns out to be overly pessimistic.

domain of incompressible flows, a set of convergence histories for Problem 2 is shown in Fig. 8c. In the study of these histories, it should be noted that a finer grid is used in Problem 2. As a result, the parameters $O^{(l)}(73)$, $O^{(l)}(109)$, $O^{(l)}(145)$, respectively, are the measures of convergence at Stations A, D, and E. A comparison between Figs. 8a and c reveals that the history of overall convergence (represented by the parameter $O^{(l)}$) for Problem 2 is very similar to that for Problem 1. Since these two problems have the same metric tensor field and the predictions of the inner loop stability analysis are dependent only on this tensor field, the similarity is a natural result of the current stability analysis. Therefore, it indicates that the inner loop stability analysis is still useful in predicting the overall convergence behavior of the inner loop iterations. On the other hand, the same comparison also reveals that the differences among the convergence histories at individual stations are much smaller in the case of Problem 2. It appears that the

interdependence between convergence at separate stations is enhanced with the introduction of a compressible flow.

As in the case of Problem 1, Problem 2 can be modified by adjusting the values of the geometric parameters c and d to $c=0.65$ and $d=0.75$. For this modified problem, iterations fail to converge during the first pass through the inner loop. This failure is not entirely unexpected since the results of the inner loop stability analysis indicate that the inner loop iterations are on the verge of instability.

The above discussions demonstrate rather convincingly that the metric tensor g_{ij} plays a key role in determining the stability and the convergence rate of the inner loop iterations. Since the metric tensor g_{ij} and the corresponding local amplification factor G_0 are functions of the coordinate transformation linking the computational domain and the physical domain, a lesson which can be drawn from the above discussions is that the coordinate transformation should be chosen such that the maximum value of G_0 in the computational domain is as small as possible. Furthermore, these discussions also point to the need to improve the current inner loop iterative procedure which becomes unstable or inefficient whenever the stability condition (B.15) of Part I is not satisfied or marginally satisfied.

To study the convergence histories during the outer loop iterations, two sets of histories corresponding, respectively, to Problems 1 and 2 are shown in Figs. 10a and b. It is noted that, in the generation of these histories, 5 inner loop iterations are executed during each pass through the inner loop. For Problem 1, the histories of $O^{(l)}$, $O^{(l)}(37)$, $O^{(l)}(55)$, and $O^{(l)}(73)$ are very similar and follow a simple pattern: The values of these parameters experience a rapid rise during the first 4 or 5 iterations. After a transition period of 2 or 3 more iterations, the initial phase of rapid increase comes to an end and is followed by a new phase of much slower increase. Based on these histories, it appears that the numerical results obtained after 10 outer loop iterations are within 1–2% of the final converged results. This assertion is also supported by the fact that the numerical results of $(\xi/2\Omega_0\theta)$

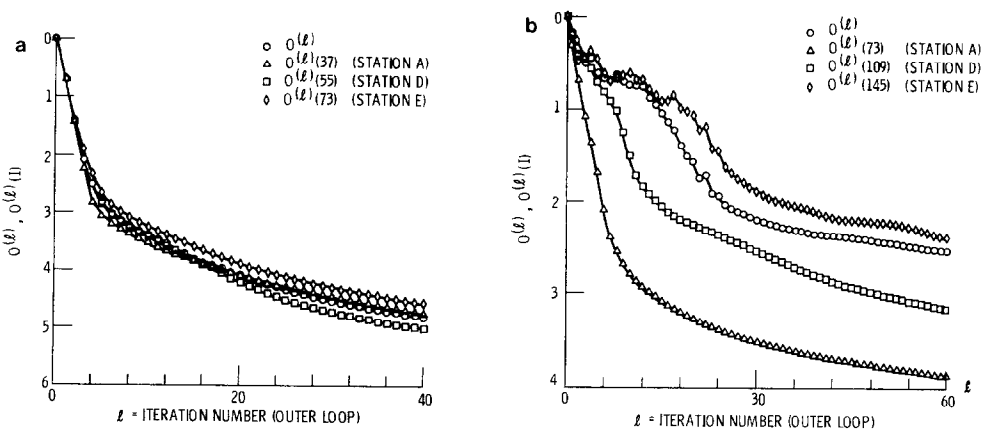

FIG. 10. Convergence histories during the outer loop iterations. (a) Problem 1. (b) Problem 2.

obtained after 10 outer loop iterations are within 1% of those obtained after 40 iterations.

For Problem 2, the convergence histories at individual stations vary widely. As shown in Fig. 10b, after only a few iterations, the convergence at Station A is far more advanced than that at Station D which, in turn, is more advanced than that at Station E. One apparent factor behind this phenomenon is the increasing complexity of the secondary flow structure occurring downstream of the channel bend (see Figs. 5a to c). This increasing complexity apparently makes it more difficult for the iterative solutions to converge at a downstream station than at an upstream station. For Problem 2, a reasonable degree of convergence may be achieved at the channel bend (Station A) with $10 \sim 20$ iterations while it may require 100–200 iterations to reach the same degree of convergence at the exit plane (Station E).

Conclusions

The numerical results obtained using the current algorithm show that it can accurately predict the behavior of weak secondary flows and is capable of generating solutions for strong secondary flows. Furthermore, it is shown that aceptable flow solutions may be obtained after only $10 \sim 20$ outer loop iterations.

An evaluation of the convergence histories during a pass through the inner loop reveals that the simple inner loop stability analysis presented in Part I is indeed a powerful tool for predicting the stability and the convergence rate of the inner loop iterations. It also points to the need to improve the current inner loop iterative procedure which is restricted by a stability condition. As a result, an improved procedure is being developed. The results of this study will be published in the near future.

APPENDIX: Inlet Flow Conditions, Outflow Conditions, and Solid Wall Conditions

In this appendix, we restrict the analysis to flows which enter the curved channel described in Section I with parallel streamlines. Such flows have inlet conditions described by the equations

$$V^1 = r(x^2, x^3), \qquad V^2 = V^3 = 0 \tag{A.1}$$

$$P = P_c \tag{A.2}$$

and

$$T = q(x^2, x^3) \tag{A.3}$$

where P_c is a constant and r, q are arbitrary functions of x^2 and x^3. As noted in Sec-

tion I, far upstream and downstream of the channel bend, the values of the metric tensor and thus the forms of fluid dynamic equations are identical in computational and physical space. As a result, Eqs. (A.1) to (A.3) are valid in both spaces. Using Eqs. (A.1) to (A.3), it can be shown that, at the inlet,

$$T_0 = q + \frac{r^2}{2C_p} \tag{A.4}$$

$$P_0 = P_c \left(1 + \frac{r^2}{2C_p \cdot q}\right)^{\gamma/(\gamma-1)} \tag{A.5}$$

With the help of Eqs. (II.1), (II.3), and (II.4) of Part I, Eqs. (A.1), (A.4), and (A.5) can be used to establish the inlet conditions for the substitute flows.

Since the streamlines of the incoming flow are parallel, the inlet streamwise vorticity Ω^1 must vanish. From Eq. (II.1) of Part I, the inlet streamwise vorticity $\Omega^{1'}$ of the corresponding substitute flow must also vanish. According to Eq. (I.19) of Part I, a choice for the inlet distributions of τ' and μ' which yields $\Omega^{1'} = 0$ at the inlet is

$$\tau' = \mu' = 0. \tag{A.6}$$

With the inlet distributions of τ' and μ' established, the solution of their respective hyperbolic equations is uniquely defined.

The construction of the appropriate inlet boundary conditions (BCs) for ψ_i, $\varphi^{(n)}$, and $\sigma^{(n)}$ is based on the assumption that the inlet flow conditions do not vary during the course of iterations. As a result, Eqs. (II.20), (II.24), and (II.26) of Part I require that, at the inlet,

$$\frac{\partial \psi_3}{\partial x^2} - \frac{\partial \psi_2}{\partial x^3} = 0,$$

$$\frac{\partial \sigma^{(n)}}{\partial x^1} = 0 \qquad (n = 3, 5, 7, \ldots), \tag{A.7}$$

and

$$\frac{\partial \varphi^{(n)}}{\partial x^1} = 0 \qquad (n = 2, 4, 6, \ldots).$$

A choice of the inlet BCs for ψ_i, $\varphi^{(n)}$, and $\sigma^{(n)}$ which is consistent with both the above conditions and Eq. (II.19) of Part I is given in the first column of Table I.

At the solid walls of the channel, we require the velocity component normal to the walls to vanish. This requirement may be expressed in the tensor form

$$V_i n^i = 0 \tag{A.8}$$

where V_i and n^i are, respectively, the covariant velocity vector and the con-

travariant normal vector at any point on the wall. For the numerical example treated in Section III, the solid walls are located at $x^2 = c$, $x^2 = d$, $x^3 = 0$, and $x^3 = e$ (see Fig. 1). From Eqs. (A.8) and (II.9) of Part I, and the fact that $g_{ij} = 0$ if $i \neq j$, the boundary conditions at these walls become

$$V_2 = F^2 = 0 \qquad \text{at } x^2 = c \text{ or } x^2 = d \tag{A.9}$$

$$V_3 = F^3 = 0 \qquad \text{at } x^3 = 0 \text{ or } x^3 = e. \tag{A.10}$$

The above BCs are satisfied by the initial flow field. According to Eqs. (II.20), (II.24), and (II.26) of Part I, they can be maintained during the course of iterations by imposing the following conditions:

(a) At $x^2 = c$ or $x^2 = d$,

$$\frac{\partial \psi_1}{\partial x^3} - \frac{\partial \psi_3}{\partial x^1} = 0,$$

$$\frac{\partial \sigma^{(n)}}{\partial x^2} = 0 \qquad (n = 3, 5, 7, \ldots) \tag{A.11}$$

and

$$\frac{\partial \varphi^{(n)}}{\partial x^2} = 0 \qquad (n = 2, 4, 6, \ldots).$$

(b) At $x^3 = 0$ or $x^3 = e$,

$$\frac{\partial \psi_2}{\partial x^1} - \frac{\partial \psi_1}{\partial x^2} = 0,$$

$$\frac{\partial \sigma^{(n)}}{\partial x^3} = 0 \qquad (n = 3, 5, 7, \ldots) \tag{A.12}$$

and

$$\frac{\partial \varphi^{(n)}}{\partial x^3} = 0 \qquad (n = 2, 4, 6, \ldots).$$

A choice of the BCs for ψ_i, $\varphi^{(n)}$, and $\sigma^{(n)}$ at the solid walls which is consistent with both the above conditions and Eq. (II.19) of Part I is given in the second and third columns of Table I.

At the channel exit, a fixed set of outflow conditions are directly imposed on the substitute flow in computational space. The initial outflow conditions are identical to the initial inlet flow conditions. The exit BCs for ψ_i, $\varphi^{(n)}$, and $\sigma^{(n)}$ are given in

the fourth column of Table I. These BCs ensure that Eq. (II.19) of Part I is satisfied, and in the limit of incompressible flow yield

$$\frac{\partial V_1^{(n)}}{\partial x^1} = 0 \tag{A.13}$$

for any n.

ACKNOWLEDGMENTS

The authors thank Dr. W. Ford, Dr. J. Pennline, and Mr. B. Auer for many valuable discussions. A particular thanks is extended to Professor E. Greitzer of the Massachusetts Institute of Technology.

REFERENCES

1. H. B. SQUIRE AND K. G. WINTER, *J. Aerosp. Sci.* **18** (1951), 271–277.
2. W. R. HAWTHORNE, *Proc. R. Soc. London Ser. A* **206** (1951), 374–387.
3. W. R. HAWTHORNE, *Proc. Cambridge Philos. Soc.* **51**, No. 4 (1955), 737–743.
4. B. LAKSHMINARAYANA AND J. H. HORLACK, *J. Fluid Mech.* **59**, Pt. 1 (1973), 97–115.
5. V. S. PRATAP AND D. B. SPALDING, *Int. J. Heat Mass Transfer* **19** (1976), 1183–1188.
6. W. R. BRILEY AND H. MCDONALD, "Analysis and Computation of Viscous Subsonic Primary and Secondary Flows," *Computational Fluid Dynamics Conference*, pp. 74–88, AIAA, 1979.
7. pressible Duct Flow. Part II - Stagnation Pressure Losses in a Rectangular Elbow," ASME Paper 79-WA/FE-5, Dec. 1979.
8. S. ABDALLAH AND A. HAMED, *AIAA J.* **19**, (8) (1981), 993–999.
9. H. LAMB, "Hydrodynamics," 6th ed., p. 205, Univ. Press, Cambridge, 1932.
10. J. ADAMS, P. SWARZTRAUBER, AND R. SWEET, "FISHPAK: Efficient FORTRAN Subprograms for the Solution of Separable Elliptic Partial Differential Equations, Version 3," Nat. Center for Atmospheric Research, Boulder, Colo., 1978.
11. M. ABRAMOWITZ AND I. A. STEGUN, "Handbook of Mathematical Functions with Formulas, Graphs, and Mathematical Tables," p. 882, Nat. Bureau of Standards, Washington, D.C., 1964.
12. G. D. SMITH, "Numerical Solution of Partial Differential Equations," Oxford Univ. Press, 1978, Eq. (4.5).